Prediction of an unusual trigonal phase of superconducting LaH$_{10}$ stable at high pressures

Ashok K. Verma ●* and P. Modak

High Pressure and Synchrotron Radiation Physics Division, Bhabha Atomic Research Centre, Mumbai 400085, India

Fabian Schrodi ●,† Alex Aperis ●, and Peter M. Oppeneer ●‡

Department of Physics and Astronomy, Uppsala University, P.O. Box 516, SE-75120 Uppsala, Sweden

Based on evolutionary crystal structure searches in combination with *ab initio* calculations, we predict an unusual structural phase of the superconducting LaH$_{10}$ that is stable from about 250 to 425 GPa pressure. However, inclusion of phonon zero-point and 300 K free-energy contributions shifts the transition pressures to higher values. This phase belongs to a trigonal $R\bar{3}m$ crystal lattice with an atypical cell angle, $\alpha_{\mathrm{rhom}} \sim 24.56°$. We find that this structure contains three units of LaH$_{10}$ in its primitive cell, unlike the previously known trigonal phase, in which the primitive cell contains only one LaH$_{10}$ unit. In this phase, a 32-H-atom cage encapsulates La atoms, analogous to the lower-pressure fcc phase. However, the hydrogen cages of the trigonal phase consist of quadrilaterals and hexagons, in contrast to the cubic phase, which exhibits squares and regular hexagons. Surprisingly, the shortest H-H distance in this phase is shorter than that of the lower-pressure cubic phase and of atomic hydrogen metal. We find a structural phase transition from trigonal to hexagonal at 492 GPa at 300 K, where the hexagonal crystal lattice coincides with earlier predictions. Solving the anisotropic Migdal-Eliashberg equations, we find that the predicted trigonal phase (for standard values of the Coulomb pseudopotential) is expected to become superconducting at a critical temperature of about 175 K, which is less than $T_c \sim 250$ K measured for cubic LaH$_{10}$.

I. INTRODUCTION

Recent collective efforts in high-pressure experiments and simulations have led to the discovery of a class of superhydride superconductors that, to date, exhibit the highest critical temperatures T_c at megabar pressures; see [1,2] for recent reviews. These superconductors are hydrogen-rich compounds, such as H$_3$S ($T_c = 203$ K at 150 GPa) [3,4], LaH$_{10\pm x}$ ($T_c \approx 250$ K in the pressure region of 137–218 GPa) [5–9], YH$_6$ ($T_c = 203$ K at 166–237 GPa) [10,11], ThH$_{10}$ ($T_c = 161$ K at 175 GPa) [12], and the recently discovered carbonaceous sulfur hydride ($T_c = 287$ K at 267 GPa) [13]. The underlying mechanism responsible for such high critical temperatures is the conventional electron-phonon coupling, which was discussed recently [5,6,14–20], even though, as has been noted, the superconducting transition is anomalously sharp [21].

Lanthanum superhydride has so far provided the highest transition temperature of the rare-earth hydrides. Its underlying crystal structure is therefore a topic of concurrent theoretical investigations [5,22–27]. Several groups have

carried out crystal structure searches, especially in the 100–300 GPa pressure region. Initial crystal searches showed that LaH$_{10}$ adopts a stable fcc lattice, $Fm\bar{3}m$, above 210 GPa, while at lower pressures the cubic phase becomes dynamically unstable [5]. However, later, a combined theoretical and experimental study identified a low-symmetry monoclinic structure, $C2/m$, as the most likely low-pressure phase [23]. In this work it was noticed that, despite the overall monoclinic crystal symmetry, the lanthanum sublattice can be described by a trigonal $R\bar{3}m$ symmetry, which was confirmed by the accompanying x-ray diffraction measurements in decompression experiments [23]. Most recently, two additional crystal structures of monoclinic $C2$ and body-centered orthorhombic $Immm$ symmetries were added to the list of possible low-pressure structures by further crystal structure searches [25]. In addition, at high pressure (>400 GPa) a hexagonal $P6_3/mmc$ structure was recently predicted [27]. It was also noted that the inclusion of anharmonic nuclear quantum corrections reduces the low-pressure, low-symmetry $C2$ and $Immm$ structures to the cubic $Fm\bar{3}m$ structure, which thus ruled out the existence of lower-symmetry structures for LaH$_{10}$ [25]. The observed $R\bar{3}m$ lanthanum sublattice, however, still awaits a satisfactory explanation. In this respect, it is pertinent to mention that former low-symmetry structures are associated with the fcc lattice through suitable deformations. The crystal structure of LaH$_{10}$ at higher pressures has not yet been fully understood, and thus, more studies in this pressure region offer an exciting possibility for the discovery of new crystal structures.

In this paper, we study the structural behavior of LaH$_{10}$ superhydride by performing evolutionary crystal structure

---

*hpps@barc.gov.in

†fabian.schrodi@physics.uu.se

‡peter.oppeneer@physics.uu.se

searches under pressure, especially above 250 GPa. We predict a phase that belongs to trigonal $R\bar{3}m$ crystal symmetry. We analyze the stability of this phase and show that it has a lower enthalpy than the previously predicted fcc $Fm\bar{3}m$ and hexagonal $P6_3/mmc$ phases. By solving the anisotropic Migdal-Eliashberg equations with *ab initio* input [28] we analyze the superconducting properties and find that the superconducting critical temperature is reduced to ~175 K, compared to $T_c = 250$ K for the cubic phase [6,8] at lower pressures, for a realistic value of the Coulomb pseudopotential ($\mu^{\star} = 0.1$). We further find that, although the electron-phonon interaction is responsible for superconductivity, the ratio $\Delta/k_B T_c$ (with Δ being the superconducting gap) deviates from the weak-coupling BCS value, placing the lanthanum superhydrides in the strong-coupling regime.

II. METHODOLOGY

To start with, we performed crystal structure searches using the evolutionary algorithm as implemented in the USPEX code [29–31]. Over the years, this method has been established as a versatile tool for predictions of novel stoichiometries and crystal structures of materials at high pressures [32–37]. We performed crystal structure searches in the pressure range of 100–500 GPa using crystal models of 1 to 4 f.u. of LaH$_{10}$. The first-generation crystal structures are always created randomly, while subsequent generations contain 20% random structures, and the remaining 80% of structures are created using heredity, soft mutation, and transmutation operators. We computed the crystal structure optimizations, enthalpies, and electronic structures within the framework of the density functional theory, while phonon dispersions and electron-phonon interactions (discussed below) were calculated within the framework of density functional perturbation theory (DFPT). All calculations employed the Perdew-Burke-Ernzerhof version of the exchange-correlation energy functional [38]. For structure optimizations and enthalpies calculations, we used the VASP code [39–42], projector augmented wave (PAW) potentials with a 600 eV plane-wave kinetic energy cutoff, and Brillouin zone (BZ) grids with a $2\pi \times 0.01$ Å^{-1} interval.

The convergence of enthalpy values with respect to the plane-wave kinetic energy cutoff and Brillouin zone grid interval was thoroughly investigated, and the results for this set of calculations are presented in the Supplemental Material [43]. We also investigated the convergence of the transition pressure value for the cubic to hexagonal phase transition with respect to these computational parameters, and we validated, furthermore, the accuracy of PAW potentials at high pressure by comparing this transition pressure value with that of all-electron full-potential calculations performed using the WIEN2K code [44]; see the Supplemental Material for details [43].

III. RESULTS

A. Structural optimization and stability

We began with 100 GPa crystal structure searches, and these searches readily reproduced previously known structures, such as fcc $Fm\bar{3}m$, trigonal (we named it trigonal-old) $R\bar{3}m$, monoclinic $C2/m$, and body-centered orthorhombic $Immm$ [7,25]. Since the low-pressure (<300 GPa) phase
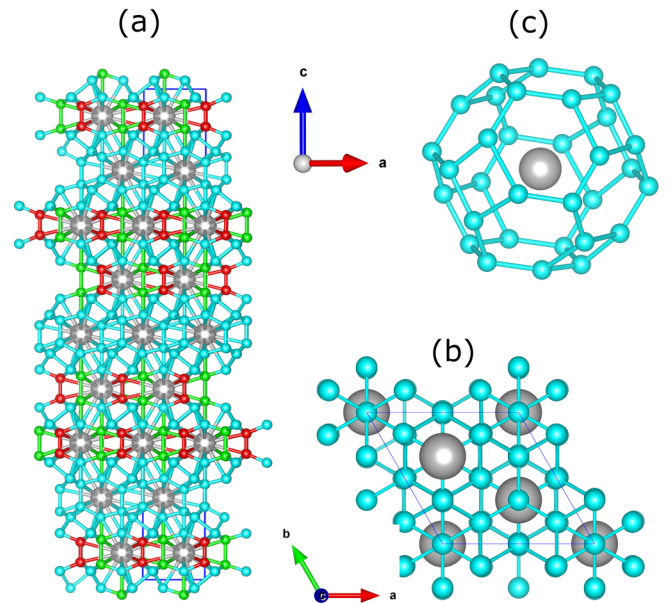
FIG. 1. (a) Ball and stick model of the discovered trigonal $R\bar{3}m$ phase, in a hexagonal setting, of superconducting LaH$_{10}$. Here, green and red bonds represent the fastest- and slowest-varying bonds under pressure, respectively. (b) Structure in the *a-b* plane. (c) A complete model of a 32-H-atom cage around the La atom. Each cage is interlinked to six other cages through cuboids wherein hydrogen atoms occupy the corner positions (not shown here). The eight hexagonal faces of each 32-H-atom cage are shared by the surrounding 32-H-atom cages (not shown here). Here, the big gray spheres represent La atoms, and small cyan spheres represent H atoms; the coordinate system shows the orientation of the crystal lattice. These structural models were rendered using the VESTA software [45].

diagram has been explored extensively in the past by many researchers, we turn our attention to the 300–500 GPa pressure region. Our crystal structure searches in this region produce two crystal structures, namely, a trigonal structure $R\bar{3}m$ and a hexagonal structure $P6_3/mmc$. The primitive cell of our trigonal structure (shown in Fig. 1) consists of 3 f.u. of LaH$_{10}$, unlike the previously known trigonal structure, which consists of only 1 f.u. of LaH$_{10}$ [5,23,25]. We also notice that our trigonal structure has an anomalously small cell angle, $\alpha_{\text{rhom}} \sim 24.56°$, unlike the earlier trigonal structure, for which $\alpha_{\text{rhom}} \sim 60°$ [5,25]. In this trigonal phase, the lanthanum atoms are surrounded by cages consisting of 32 H atoms, each of which is linked to six neighboring cages via cuboids of 8 H atoms. The eight hexagonal faces of each 32-H-atom cage are shared by the surrounding 32-H-atom cages. Contrary to the low-pressure cubic phase, the hydrogen cage in the trigonal structure is made of quadrilaterals and hexagons, as shown in Fig. 1.

Interestingly, our trigonal phase has slightly lower enthalpy (<2.0 meV/atom) than the fcc phase even for lower pressures (<250 GPa), thus making these phases energetically indistinguishable in this pressure region. In addition, the previously mentioned argument that nuclear quantum corrections (zero-point vibrations) of hydrogen destabilize low-symmetry structures in favor of the cubic $Fm\bar{3}m$ structure [25] could play a role here. However, the enthalpy difference between
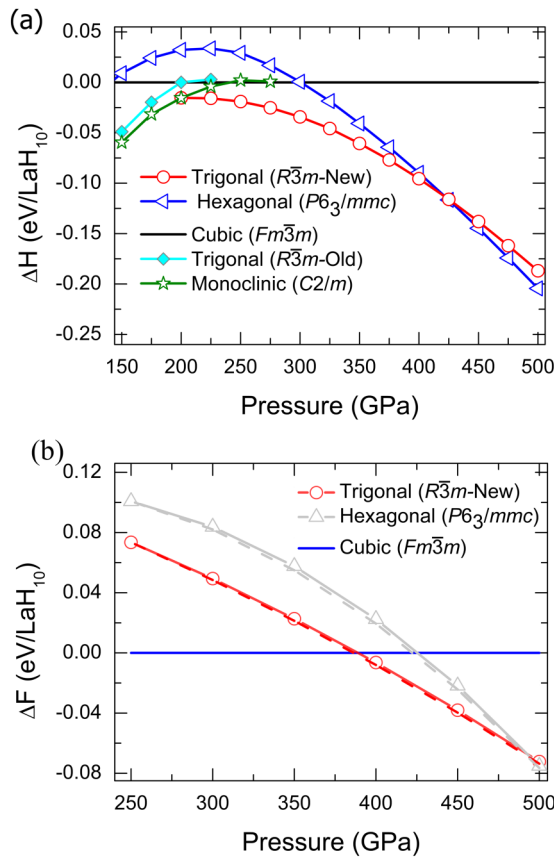
FIG. 2. (a) Computed enthalpy difference of trigonal and hexagonal structures of LaH$_{10}$ with reference to the fcc structure (black line). Results for the monoclinic ($C2/m$) and previously reported trigonal ($R\bar{3}m$) phases are also shown. (b) Free-energy difference ΔF of these two structure with reference to the fcc structure. Here, solid lines represent phonon zero-point results, and dashed lines represent 300 K results.

trigonal and cubic phases grows with increasing pressure, reaching a value of $\sim$9.0 meV/atom at 400 GPa, as shown in Fig. 2(a). We also find that our trigonal phase transforms to a hexagonal phase above 425 GPa. Our hexagonal phase belongs to the same crystal lattice ($P6_3/mmc$) as that of previous work [27]. For the trigonal phase, we obtain (in a hexagonal setting) $a = b = 3.812$ Å and $c = 23.0467$ Å at 350 GPa. Corresponding Wyckoff positions are 3b, (0.0000, 0.0000, 0.5000) for La1; 6c, (0.0000, 0.0000, 0.7213), for La2; 6c, (0.0000, 0.0000, 0.8055), for H1; 6c, (0.0000, 0.0000, 0.4147), for H2; 18h, (08276, 0.1734, 0.2059), for H3; 18h, (0.1656, 0.8343, 0.0944), for H4; 18h, (0.1658, 0.8342, 0.0174), for H5; 6c, (0.0000, 0.0000, 0.0348), for H6; 6c, (0.0000, 0.0000, 0.6356), for H7; 6c, (0.0000, 0.0000, 0.8513), for H8; and 6c, (0.0000, 0.0000, 0.0766), for H9.

We estimated the effects of phonons on the phase stability of the cubic, trigonal, and hexagonal phases by computing the phonon free energies as a function of pressure for these structures. The results of this study are presented in Fig. 2(b). Here, we have not computed the phonon free energies for the trigonal-old and C_2/m structures as these structures were already shown to become energetically unfavorable with the addition of the phonon effect [27]. Although phonon
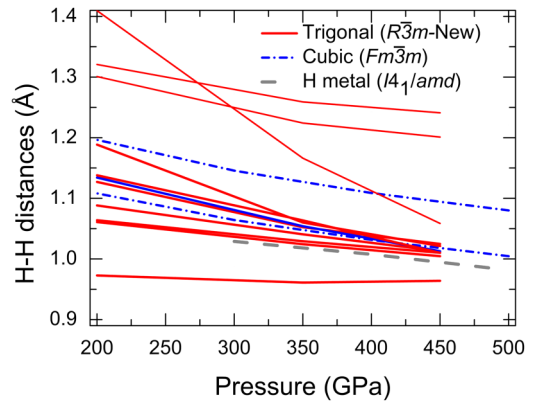

FIG. 3. Comparison of H-H distances as a function of pressure in the fcc and trigonal structures along with atomic hydrogen metal [46].

zero-point contributions shift the cubic to trigonal and trigonal to hexagonal transition pressures to higher values, the structural sequence remains unaltered. The addition of phonon zero-point (300 K) free-energy contributions changes the cubic to trigonal transition pressure to 389 (386) GPa, whereas the trigonal to hexagonal transition pressure changes to 493 (492) GPa. Our value for the cubic to hexagonal transition pressure, 422 GPa, with 300 K phonon effects included agrees well with the previously reported value of 420 GPa [27].

We did not find any other lower-enthalpy structure up to pressures of 500 GPa. Similar to the cubic $Fm\bar{3}m$ phase, the trigonal phase also has a 32-H-atom cage around the La atoms [see Fig. 1(b)]. However, square and hexagonal faces are now distorted, probably to accommodate the symmetry changes. Here, the square and regular hexagonal faces of the cubic H cage deform into quadrilateral and irregular hexagonal faces [7]. As shown in Fig. 3, this leads to a splitting of the two H-H distances of the fcc phase into many different H-H distances. Notably, the smallest H-H distances are smaller than those of the cubic phase as well as those of hydrogen metal at similar pressures [46].

We now turn our attention to the electronic and phonon properties of our phase. They were calculated using DFPT as implemented in the QUANTUM ESPRESSO package [47]. We use ultrasoft pseudopotentials with 50 and 500 Ry cutoffs for the plane-wave kinetic energy and charge density, respectively. We used a 24 $\times$ 24 $\times$ 24 Monkhorst-Pack [48] **k**-point grid for the electronic properties and a 12 $\times$ 12 $\times$ 12**k**-point mesh for the phonons. Force constants, phonons, and electron-phonon couplings were calculated on a 4 $\times$ 4 $\times$ 4 **q**-point mesh. A test run with denser 36 $\times$ 36 $\times$ 36 **k**-point meshes did not show significant changes.

In Fig. 4 we show the electronic band structure and density of states (DOS) at 350 GPa. The electronic band structure clearly shows that the trigonal phase is a good metal, similar to the lower-pressure cubic phase. Many electronic bands cross the Fermi level along various directions of the BZ [see Fig. 4(a)]. The orbital projection of the DOS reveals that La f, La d, and La p states contribute most to the DOS at the Fermi level, while La s contributions are insignificant and hence are not shown in the plot. Similar DOS trends were also
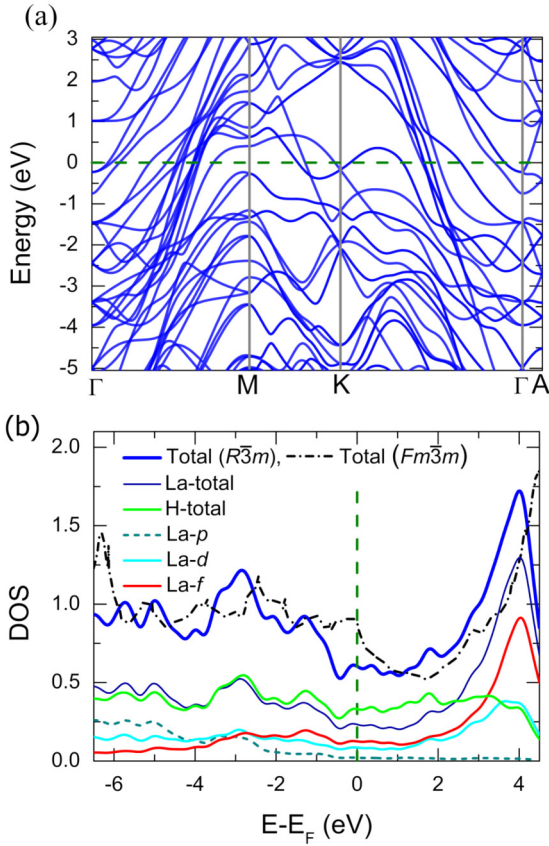
FIG. 4. (a) Electronic band structure of the trigonal $R\bar{3}m$ structure, in a hexagonal setting, along the high-symmetry directions of the Brillouin zone at 350 GPa. (b) Total density of states (DOS) and atom projected partial density of states (PDOS). Here, total DOS is given in units of states/eV per LaH_{10} unit, and PDOSs are given in units of states/eV per atom. Contributions of La s states are insignificant to the total DOS values at the Fermi level and hence are not shown. The La PDOSs represent the average contribution of two types of atoms, and the La total represents the sum of these PDOSs. The H total represents the sum of s DOSs of all 10 H atoms. For comparison, the total DOS for the cubic $Fm\bar{3}m$ phase is also shown. Vertical and horizontal dashed lines in (a) and (b), respectively, show the position of the Fermi level.

noticed for the cubic phase [5]. However, the trigonal phase has considerably smaller DOS values (N_0) at the Fermi level than the cubic phase. For example, at 350 GPa we compute $N_0 = 0.60$ states/eV and $N_0 = 0.88$ states/eV per LaH_{10} unit for the trigonal and cubic phases, respectively.

The phonon dispersions of the trigonal phase are shown in Fig. 5(a) along high-symmetry lines of the BZ, and the respective phonon density of states is shown in Fig. 5(b). It is pertinent to mention that the highest phonon frequency (~ 2500 cm^{-1}) of this phase lies between the highest frequencies of the cubic phase and of the atomic hydrogen metal. These phonon frequencies are ~ 2000 cm^{-1} at 300 GPa [5] and ~ 2600 cm^{-1} at 400 GPa [46] for the cubic LaH_{10} and hydrogen metal, respectively. Evidently, the La atoms contribute mainly to the low-frequency part of the phonon spectrum, below 500 cm^{-1}, whereas H atoms contribute mainly to the high-frequency part of the phonon spectrum, as can be seen in Fig. 5(b).
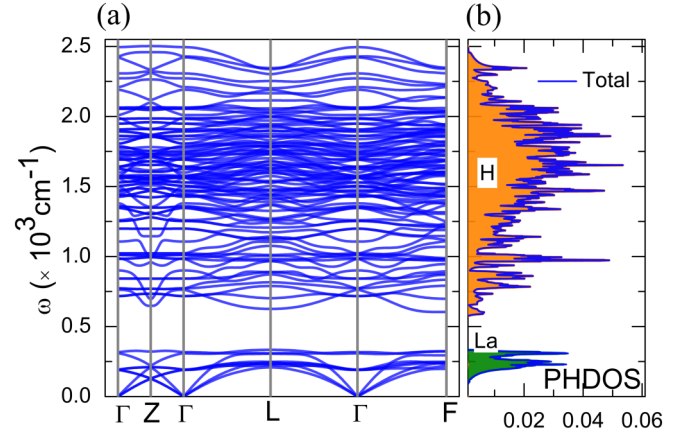

FIG. 5. (a) Phonon dispersions computed for the primitive trigonal unit cell along high-symmetry lines of the Brillouin zone. (b) The corresponding phonon density of states (PHDOS). Here, the total phonon DOS represents the contribution of a single LaH_{10} unit. Olive and orange shaded regions represent the total phonon DOS of the La and H atoms, respectively.

B. Superconducting properties

Next, we calculate the superconducting properties of the discovered trigonal phase at 350 GPa by numerically solving the anisotropic Migdal-Eliashberg equations,

$$Z_{\mathbf{k},m} = 1 + \frac{\pi T}{\omega_m} \sum_{\mathbf{k}',m'} \frac{\delta(\xi_{\mathbf{k}'})}{N_0} \lambda_{\mathbf{k}-\mathbf{k}',m-m'} \frac{\omega_{m'}}{\sqrt{\omega_{m'}^2 + \Delta_{\mathbf{k}',m'}^2}}, \quad (1)$$

$$\Delta_{\mathbf{k},m} = \frac{\pi T}{Z_{\mathbf{k},m}} \sum_{\mathbf{k}',m'} \frac{\delta(\xi_{\mathbf{k}'})}{N_0} [\lambda_{\mathbf{k}-\mathbf{k}',m-m'} - \mu^{\star}(\omega_c)]$$
$$\times \frac{\Delta_{\mathbf{k}',m'}}{\sqrt{\omega_{m'}^2 + \Delta_{\mathbf{k}',m'}^2}}, \quad (2)$$

as implemented in the Uppsala Superconductivity code (UP-PSC) [28,49–52]. In the above equations, $Z_{\mathbf{k},m}$ and $\Delta_{\mathbf{k},m}$ are the mass renormalization and superconducting gap function,
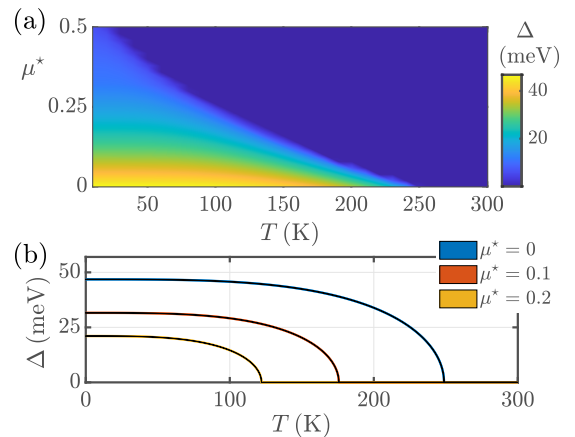

FIG. 6. (a) Self-consistently calculated maximum superconducting gap Δ as a function of temperature and screened Coulomb potential $\mu^{\star}$. (b) Temperature-dependent Δ computed for three values of $\mu^{\star}$ as written in the legend. The thickness of each curve reflects the momentum anisotropy of the superconducting gap.

TABLE I. Characteristic superconducting properties of trigonal LaH_{10} computed for different values of the Coulomb pseudopotential $\mu^\star$ at a pressure of 350 GPa.

$\mu^\star$	T_c (K)	Δ_0 (meV)	$\Delta_0/k_B T_c$	T_c^{AD} (K)
0	248.7	46.9	2.19	231
0.1	175.5	31.6	2.09	184
0.2	122.0	21.1	2.01	136

respectively. Equations (1) and (2) are solved self-consistently in Matsubara space [with fermionic Matsubara frequency $\omega_m = \pi T(2m + 1)$, $m \in \mathbb{Z}$], as a function of the temperature T and Anderson-Morel Coulomb pseudopotential $\mu^\star$. The dynamic electron-phonon coupling is calculated via $\lambda_{\mathbf{q},l} = \sum_\nu \lambda_{\mathbf{q},\nu} \omega_{\mathbf{q},\nu}^2 / (\omega_{\mathbf{q},\nu}^2 + q_l^2)$, with $q_l = 2\pi T l$ ($l \in \mathbb{Z}$) being the bosonic Matsubara frequencies. The electron energies $\xi_{\mathbf{k}}$, density of states at the Fermi level N_0, phonon frequencies $\omega_{\mathbf{q},\nu}$ (ν branch index), and electron-phonon couplings $\lambda_{\mathbf{q},\nu}$ are obtained from the above-described *ab initio* calculations. The total electron-phonon coupling λ is given by $\lambda = \sum_{\mathbf{q},\nu} \lambda_{\mathbf{q},\nu}$.

In Fig. 6(a) we show the maximum zero-frequency superconducting gap $\Delta = \max_{\mathbf{k}} \Delta_{\mathbf{k},m=0}$ as a function of T and $\mu^\star$. For small values of the Coulomb pseudopotential, Δ reaches around 45 meV in the limit $T \to 0$. Considering a very wide range of $\mu^\star$, the critical temperatures range from 30 K to approximately 250 K. For closer inspection we choose three specific values, $\mu^\star \in \{0, 0.1, 0.2\}$, that are close to the archetypal value $\mu^\star = 0.1$ and plot the temperature dependence of Δ in Fig. 6(b). As a measure of momentum anisotropy of the gap, we show here the range $[\min_{\mathbf{k}} \Delta_{\mathbf{k},m=0}, \max_{\mathbf{k}} \Delta_{\mathbf{k},m=0}]$ for each $\mu^\star$ and T. As is directly apparent, each shaded area in Fig. 6(b) is very thin, reflecting a negligible degree of gap anisotropy, a property which is in line with results for most hydride superconductors. The critical temperature for the typical value of $\mu^\star = 0.1$ [5,6,14,16] is approximately 175 K, which is a significant decrease compared to $T_c \leqslant 250$ K in the lower-pressure cubic phase of LaH_{10} [5,8]. This change in T_c can partially be understood in terms of the different values for the DOS at the Fermi energy N_0 in the trigonal and cubic phases, as mentioned before. Additionally, the electron-phonon coupling strength $\lambda = 1.69$ as found here is smaller than the value of $\lambda = 2.2$ that was estimated for the cubic phase at 250 GPa [5]. It also must be mentioned that suitably doping LaH_{10} could provide an increase in the Fermi-energy DOS and hence enhance T_c [53].

In Table I we list some characteristics of the superconducting state for the same values of the Coulomb pseudopotential. The limiting values $\Delta_0 = \Delta(T = 0)$ were obtained via the fitting function $\Delta(T) \simeq \mathrm{Re}\sqrt{\alpha - T^\beta/\gamma}$. Remarkably, for all choices of $\mu^\star$ we find the ratio $\Delta/k_B T_c$ in the strong-coupling regime, in contrast to the weak-coupling BCS value of 1.76. Thus, although the electron-phonon interaction is prevalent, lanthanum superhydride cannot be considered a BCS

superconductor. Finally, we compare our values for T_c with the critical temperatures T_c^{AD} as obtained from the modified McMillan equation by Allen and Dynes [54]; see the Supplemental Material for details [43]. It turns out that both critical temperatures are very similar for each value of $\mu^\star$, which can be associated with the very isotropic nature of the superconducting state [see Fig. 6(b)]. A similar consistency between critical temperatures obtained from the (isotropic) Eliashberg equations and the Allen-Dynes equation was observed previously for actinium superhydrides [55]. The fact that reasonably accurate critical temperatures are obtained with the Allen-Dynes equation could be beneficial for machine learning techniques to search for hydrogen-based compounds with record high T_c [56–58].

IV. CONCLUSIONS

In summary, we have predicted a different trigonal phase of superconducting LaH_{10} at pressures above 250 GPa. This phase has an anomalously small cell angle, and its primitive cell is made of three units of LaH_{10}, unlike the previously known trigonal phase, in which only one unit of LaH_{10} resides in the primitive cell. Analogous to the lower-pressure cubic phase, this phase also has a 32-H-atom cage encapsulating the lanthanum atom, and each cage is interconnected to the six neighboring such cages. However, the crystal symmetry reduction from cubic to trigonal results in significant distortions of the hydrogen cages around the La atoms. Interestingly, the smallest H-H distances in the trigonal phase are smaller than those of the cubic phase and those of an atomic hydrogen metal. We have also found that the trigonal phase transforms to a hexagonal phase, where the crystal lattice is identical to that given by earlier predictions. Including phonon free energies, at both $T = 0$ and 300 K, we found that the transition pressures shift to higher values. Solving the anisotropic Migdal-Eliashberg equations on the basis of *ab initio* input, we predicted strong-coupling superconductivity with a high transition temperature, $T_c \approx 175$ K, for the archetypal value $\mu^\star = 0.1$ at 350 GPa, a T_c value which is thus somewhat lower than the value of $T_c \approx 250$ K that was measured [8] and computed [5] for the cubic LaH_{10} phase.

[1] C. J. Pickard, I. Errea, and M. I. Eremets, Annu. Rev. Condens. Matter Phys. **11**, 57 (2020).

[2] J. A. Flores-Livas, L. Boeri, A. Sanna, G. Profeta, R. Arita, and M. I. Eremets, Phys. Rep. **856**, 1 (2020).

[3] D. Duan, Y. Liu, F. Tian, D. Li, X. Huang, Z. Zhao, H. Yu, B. Liu, W. Tian, and T. Cui, Sci. Rep. **4**, 6968 (2014).

[4] A. P. Drozdov, M. I. Eremets, I. A. Troyan, V. Ksenofontov, and S. I. Shylin, Nature (London) **525**, 73 (2015).

[5] H. Liu, I. I. Naumov, R. Hoffmann, N. W. Ashcroft, and R. J. Hemley, Proc. Natl. Acad. Sci. USA **114**, 6990 (2017).

[6] F. Peng, Y. Sun, C. J. Pickard, R. J. Needs, Q. Wu, and Y. Ma, Phys. Rev. Lett. **119**, 107001 (2017).

[7] M. Somayazulu, M. Ahart, A. K. Mishra, Z. M. Geballe, M. Baldini, Y. Meng, V. V. Struzhkin, and R. J. Hemley, Phys. Rev. Lett. **122**, 027001 (2019).

[8] A. P. Drozdov, P. P. Kong, V. S. Minkov, S. P. Besedin, M. A. Kuzovnikov, S. Mozaffari, L. Balicas, F. F. Balakirev, D. E. Graf, V. B. Prakapenka, E. Greenberg, D. A. Knyazev, M. Tkacz, and M. I. Eremets, Nature (London) **569**, 528 (2019).

[9] D. Sun, V. S. Minkov, S. Mozaffari, S. Chariton, V. B. Prakapenka, M. I. Eremets, L. Balicas, and F. F. Balakirev, arXiv:2010.00160.

[10] I. A. Troyan, D. V. Semenok, A. G. Kvashnin, A. V. Sadakov, O. A. Sobolevskiy, V. M. Pudalov, A. G. Ivanova, V. B. Prakapenka, E. Greenberg, A. G. Gavriliuk, I. S. Lyubutin, V. V. Struzhkin, A. Bergara, I. Errea, R. Bianco, M. Calandra, F. Mauri, L. Monacelli, R. Akashi, and A. R. Oganov, Advanced Materials **33**, 2006832 (2021).

[11] P. Kong, V. S. Minkov, M. A. Kuzovnikov, A. P. Drozdov, S. P. Besedin, S. Mozaffari, L. Balicas, F. F. Balakirev, V. B. Prakapenka, S. Chariton, D. A. Knyazev, E. Greenberg, and M. I. Eremets, Nat. Commun. **12**, 5075 (2021).

[12] D. V. Semenok, A. G. Kvashnin, A. G. Ivanova, V. Svitlyk, V. Y. Fominski, A. V. Sadakov, O. A. Sobolevskiy, V. M. Pudalov, I. A. Troyan, and A. R. Oganov, Mater. Today **33**, 36 (2020).

[13] E. Snider, N. Dasenbrock-Gammon, R. McBride, M. Debessai, H. Vindana, K. Vencatasamy, K. V. Lawler, A. Salamat, and R. P. Dias, Nature (London) **586**, 373 (2020).

[14] H. Liu, I. I. Naumov, Z. M. Geballe, M. Somayazulu, J. S. Tse, and R. J. Hemley, Phys. Rev. B **98**, 100102(R) (2018).

[15] A. P. Durajski, C. Wang, Y. Li, R. Szcześniak, and J.-H. Cho, Ann. Phys. (Berlin, Ger.) **533**, 2000518 (2020).

[16] W. Sun, X. Kuang, H. D. J. Keen, C. Lu, and A. Hermann, Phys. Rev. B **102**, 144524 (2020).

[17] C. Wang, S. Yi, and J.-H. Cho, Phys. Rev. B **101**, 104506 (2020).

[18] D. A. Papaconstantopoulos, M. J. Mehl, and P.-H. Chang, Phys. Rev. B **101**, 060506(R) (2020).

[19] W. Cui, T. Bi, J. Shi, Y. Li, H. Liu, E. Zurek, and R. J. Hemley, Phys. Rev. B **101**, 134504 (2020).

[20] Y. Sun, Y. Tian, B. Jiang, X. Li, H. Li, T. Iitaka, X. Zhong, and Y. Xie, Phys. Rev. B **101**, 174102 (2020).

[21] J. E. Hirsch and F. Marsiglio, Phys. Rev. B **103**, 134505 (2021).

[22] Y. Li, J. Hao, H. Liu, J. S. Tse, Y. Wang, and Y. Ma, Sci. Rep. **5**, 9948 (2015).

[23] Z. M. Geballe, H. Liu, A. K. Mishra, M. Ahart, M. Somayazulu, Y. Meng, M. Baldini, and R. J. Hemley, Angew. Chem., Int. Ed. **57**, 688 (2018).

[24] C. Wang, S. Yi, and J.-H. Cho, Phys. Rev. B **100**, 060502(R) (2019).

[25] I. Errea, F. Belli, L. Monacelli, A. Sanna, T. Koretsune, T. Tadano, R. Bianco, M. Calandra, R. Arita, F. Mauri, and J. A. Flores-Livas, Nature (London) **578**, 66 (2020).

[26] I. A. Kruglov, D. V. Semenok, H. Song, R. Szcześniak, I. A. Wrona, R. Akashi, M. M. Davari Esfahani, D. Duan, T. Cui, A. G. Kvashnin, and A. R. Oganov, Phys. Rev. B **101**, 024508 (2020).

[27] A. M. Shipley, M. J. Hutcheon, M. S. Johnson, R. J. Needs, and C. J. Pickard, Phys. Rev. B **101**, 224511 (2020).

[28] A. Aperis, P. Maldonado, and P. M. Oppeneer, Phys. Rev. B **92**, 054516 (2015).

[29] A. R. Oganov and C. W. Glass, J. Chem. Phys. **124**, 244704 (2006).

[30] A. O. Lyakhov, A. R. Oganov, H. T. Stokes, and Q. Zhu, Comput. Phys. Commun. **184**, 1172 (2013).

[31] A. R. Oganov, A. O. Lyakhov, and M. Valle, Acc. Chem. Res. **44**, 227 (2011).

[32] A. R. Oganov and S. Ono, Nature (London) **430**, 445 (2004).

[33] P. Modak and A. K. Verma, Phys. Chem. Chem. Phys. **21**, 13337 (2019).

[34] A. K. Verma and P. Modak, Phys. Chem. Chem. Phys. **20**, 26344 (2018).

[35] A. K. Verma, P. Modak, and L. Stixrude, Amer. Mineral. **103**, 1906 (2018).

[36] A. K. Verma, P. Modak, and S. M. Sharma, J. Alloys Compd. **710**, 460 (2017).

[37] N. N. Patel, A. K. Verma, A. K. Mishra, M. Sunder, and S. M. Sharma, Phys. Chem. Chem. Phys. **19**, 7996 (2017).

[38] J. P. Perdew, K. Burke, and M. Ernzerhof, Phys. Rev. Lett. **77**, 3865 (1996).

[39] G. Kresse and J. Hafner, J. Phys.: Condens. Matter **6**, 8245 (1994).

[40] P. E. Blöchl, Phys. Rev. B **50**, 17953 (1994).

[41] G. Kresse and J. Furthmüller, Comput. Mater. Sci. **6**, 15 (1996).

[42] G. Kresse and D. Joubert, Phys. Rev. B **59**, 1758 (1999).

[43] See Supplemental Material at http://link.aps.org/supplemental/10.1103/PhysRevB.104.174506, which includes Ref. [59], for enthalpy and transition pressure convergence tests with respect to the Brillouin zone mesh interval and plane-wave kinetic energy cutoff, for a comparison of the transition pressure data of PAW potentials with all-electron WIEN2K data, and also for the calculation of the critical temperature.

[44] P. Blaha, K. Schwarz, G. Madsen, D. Kvasnicka, J. Luitz, R. Laskowski, F. Tran, and L. D. Marks, *WIEN2k: An Augmented Plane Wave Plus Local Orbitals Program for Calculating Crystal Properties* (Technische Universität Wien, Vienna, 2019).

[45] K. Momma and F. Izumi, J. Appl. Crystallogr. **44**, 1272 (2011).

[46] A. K. Verma, P. Modak, F. Schrodi, A. Aperis, and P. M. Oppeneer, Phys. Rev. B **103**, 094505 (2021).

[47] P. Giannozzi, J. Phys.: Condens. Matter **21**, 395502 (2009).

[48] H. J. Monkhorst and J. D. Pack, Phys. Rev. B **13**, 5188 (1976).

[49] The Uppsala Superconductivity (UPPSC) code provides a package to self-consistently solve the anisotropic, multiband, and full-bandwidth Eliashberg equations for frequency-even and -odd superconductivity mediated by phonons, charge fluctuations, or spin fluctuations on the basis of *ab initio* calculated input.

[50] F. Schrodi, A. Aperis, and P. M. Oppeneer, Phys. Rev. B **99**, 184508 (2019).

[51] F. Schrodi, P. M. Oppeneer, and A. Aperis, Phys. Rev. B **102**, 024503 (2020).

[52] F. Schrodi, A. Aperis, and P. M. Oppeneer, Phys. Rev. B **102**, 014502 (2020).

[53] J. A. Flores-Livas, T. Wang, T. Nomoto, T. Koretsune, Y. Ma, R. Arita, and M. Eremets, arXiv:2010.06446.

[54] P. B. Allen and R. C. Dynes, Phys. Rev. B **12**, 905 (1975).

[55] D. V. Semenok, A. G. Kvashnin, I. A. Kruglov, and A. R. Oganov, J. Phys. Chem. Lett. **9**, 1920 (2018).

[56] V. Stanev, C. Oses, A. G. Kusne, E. Rodriguez, J. Paglione, S. Curtarolo, and I. Takeuchi, npj Comput. Mater. **4**, 29 (2018).

[57] T. Ishikawa, T. Miyake, and K. Shimizu, Phys. Rev. B **100**, 174506 (2019).

[58] P. Song, Z. Hou, P. B. de Castro, K. Nakano, K. Hongo, K. Hongo, Y. Takano, and R. Maezono, arXiv:2103.00193.

[59] M. Methfessel and A. T. Paxton, Phys. Rev. B **40**, 3616 (1989).